An approximate Riemann solver for shallow water equations and heat advection in horizontal centrifugal casting

Jan Boháček [a,*], Abdellah Kharicha [b], Andreas Ludwig [a], Menghuai Wu [b]

[a] Department of Metallurgy, Montanuniversitaet Leoben, Franz-Joseph Strasse 18, 8700 Leoben, Austria
[b] Christian Doppler Lab for Advanced Simulation of Solidification and Melting, Dept. of Metallurgy, Montanuniversitaet Leoben, Franz-Joseph Strasse 18, 8700 Leoben, Austria

ARTICLE INFO

ABSTRACT

An approximate Riemann solver was developed for solving modified shallow water equations (SWE) and energy transport describing the average flow dynamics of a single layer spreading inside a horizontally rotating cylinder. The numerical model was particularly developed for simulating the horizontal centrifugal casting (HSC) of the outer shell of a work roll. The SWE were derived in the rotating frame of reference; therefore, fictitious forces (the centrifugal force and the Coriolis force) were considered. In addition, other forces such as the bed shear force, the force of gravity, the wind shear force and forces arising from the variable liquid/solid interface were taken into account. The Jacobian matrix of the nonlinear hyperbolic system of PDEs was decomposed into a set of eigenvalues and corresponding eigenvectors using standard and corrected Roe averages. A Harten–Hyman entropy fix was used to prevent expansion shocks (entropy violating solutions) typically occurring during transonic rarefactions. Source terms were applied as a stationary discontinuity and were physically bounded and well-balanced for steady states (producing non-oscillatory solutions). Each wave was upwinded using the explicit Godunov's method. The high resolution corrections with flux limiters were used to achieve second order of accuracy and dispersion free solutions at discontinuities. In addition to the Riemann solver, a central scheme FV model was used to solve the heat diffusion inside the cylinder (mold) and partially solidified liquid layer, coupled with the solidification model. Several simulations were performed, results were analyzed and discussed.

© 2015 The Authors. Published by Elsevier Inc. This is an open access article under the CC BY-NC-ND license (http://creativecommons.org/licenses/by-nc-nd/4.0/).

1. Introduction

The present paper describes in detail an approximate Riemann solver for solving modified shallow water equations and energy transport of a single liquid layer spreading inside a horizontally rotating cylinder. The horizontal centrifugal casting (HSC) of the outer shell of a work roll is an industrial application of such a process. In brief, the HSC process (Fig. 1) can be summarized as the following: A cylindrical mold is horizontally placed on four carrying rollers, from which two coaxial are always driven, whereas other two are driving. While the mold is rotating at a high speed (~600 rpm), a liquid metal is poured from the crucible via the statically mounted runner approximately in the center of the mold. Due to high centrifugal forces the liquid metal spreads uniformly and creates a sleeve of a constant thickness. This particular process of casting a work roll
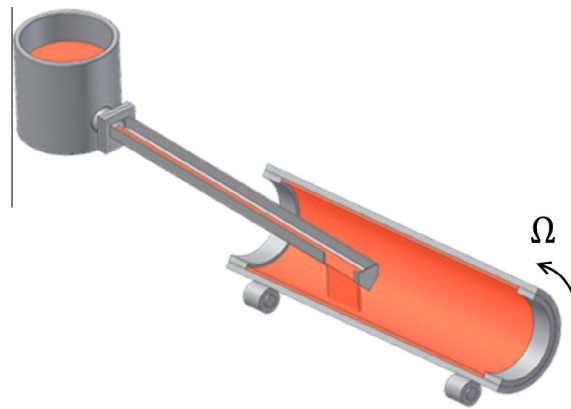
Fig. 1. A schematic of the horizontal centrifugal casting.

takes approximately 35 min. Generally, a centrifugally cast product has a superior mechanical properties compared to conventional gravitational castings [1].

Among other research papers published recently, mathematical models differ mainly in whether the flow was solved or not. Numerical studies solving the flow dynamics were mostly using the VOF method [2] to capture the interface between the liquid layer and the surrounding air. The simulations performed by Xu [3] were terminated at 30 s and thus; only the filling stage of the casting could be analyzed. In the paper, the time dependent distribution of the surface temperature on the external mold wall was obviously the main objective. The solidification model was not however mentioned in the text. Another interesting paper by Kaschnitz [4] presented a HSC simulation of seamless pipes performed using the commercial package FLOW3D. In order to avoid extremely low time steps, momentum equations were solved in the rotating frame of reference. However, due to a very small wall-to-length thickness ratio, one simulation still took considerably long time (∼20 days). A commercial code (STAR-CD V4) was used also in a work done by Prasad [5]. The mesh inside the mold was entirely constructed out of rather coarse polyhedral elements, which allowed notably large time steps (∼0.01 s). Only the continuity and momentum equations were solved for the flow. Heat transfer and solidification were not discussed in the paper. Results from simulations showed roughly how the melt is spreading during the filling stage, however no details are given on how the filling was imposed and whether the model could capture some free surface patterns or not. It can be concluded that such multiphase (VOF) simulations can successfully resolve a flow field of the liquid metal during the HSC process, however; only a limited period of time is usually concerned. Moreover, these simulations are solely covering the topic of solidification of the liquid layer. On the other hand, several research papers can be found dealing with the complete solidification of the liquid layer yet omitting the flow. The main object of consideration is a time dependent thickness of the solidifying shell often influenced by a segregation of some element due to a density difference and extremely high centrifugal pressure. For example in [6], Drenchev introduced a numerical model discussing some aspects of macrosegregation of reinforcing particles in a metal matrix. The enthalpy equation was the primary equation to solve with thermal physical properties determined from the segregation model. Since the flow (or the mold filling) was not included, the initial thickness of the liquid layer was uniform and identical to the final thickness of the shell. Similar numerical models can be found in [7,8]. The main bottleneck is the fact that the model lacks variances in the mold and shell temperatures due to the localized filling, which in turn affects the local thickness of the solidified shell and the macrostructure pattern consequently.

In the present paper, a fruitful effort was made to develop a novel approach, which would take the flow into consideration and still allow for a complete solidification of the shell in a reasonable computational time. The flow during the HSC process can be characterized as a free surface flow, in which the thickness of the liquid layer is rather small compared to the length of the mold. For this reason, it is rational to expect the momentum in the radial direction to be negligible compared to the momentum in the axial and tangential direction. Taking the 3D Euler equations and the continuity equation leaving out the momentum in the radial direction, integrating momentum and mass equations along the liquid height, and applying kinematic boundary condition on the free surface one obtains the 2D shallow water equations (SWE) originally derived in [9]. From the asymptotic series of the static pressure only the first term, the hydrostatic pressure is considered and terms with higher derivatives are neglected. This as a hydrostatic condition is a leading order approximation to the static pressure and is relevant for flows where a horizontal scale L is large compared to a characteristic height H. Note that no assumption is made about amplitudes of waves on the free surface. All the nonlinearities are retained. The original SWE are strictly hyperbolic nonlinear PDEs. In the following text, the SWE are modified to describe the average flow dynamics of the liquid layer inside the horizontally rotating cylinder. Next, an approximate Riemann solver is derived and carefully detailed. Several 1D numerical tests are shown in order to demonstrate the capability of the Riemann solver. In addition, 2D numerical examples are presented showing the simulation of the HSC process. Note that the approximate Riemann solver is used to solve the SWE and the heat advection within the liquid layer. An additional central difference FV model is used to calculate the heat

diffusion and solidification, which is not covered in the present paper. Details about the heat transfer and solidification model are discussed in [10].

2. Theory

2.1. Original form of shallow water equations

The shallow water equations (SWE) are suitable for a numerical description of so-called gravity waves i.e. waves formed and propagated under action of the gravitational acceleration. The SWE are typically applied in modeling of oceanography [11] and river flows [12]. The SWE can effectively and accurately predict the speed and the amplitude of a propagating tsunami, a tidal bore or any other wave until it breaks into a 3D flow structure [13]. In a 2D Cartesian coordinate system, the continuity and momentum equations take the following form:

$$h_t + (hu)_x + (hv)_y = 0 \tag{1}$$

and

$$
\begin{aligned}
(hu)_t + \left(hu^2 + \frac{1}{2}gh^2 \right)_x + (huv)_y &= 0 \\
(hv)_t + (huv)_x + \left(hv^2 + \frac{1}{2}gh^2 \right)_y &= 0
\end{aligned}
\tag{2}
$$

where h is the liquid height, g is the gravitational acceleration, and u, v are the mass-flow averaged velocity components in the x- and y-direction, respectively. Note that the indices t, x, and y represent temporal and spatial derivatives. Usually, the SWE are solved in the homogeneous form (1), (2). Sometimes, it is however necessary to include momentum source terms such as the bed shear force, wind shear force, etc. In addition, some applications e.g. modeling of landslides require a multilayer approach. In that case, different SWE are used for each layer and coupling terms provide the desired interaction between these layers [14].

2.2. Modified shallow water equations

The original SWE (1), (2) were modified to simulate the average flow dynamics of the liquid layer spreading inside a horizontally rotating cylinder. During the observation of the real casting, the liquid melt seems to quickly pick up the speed of the rotating mold [15]. Therefore, the choice of the rotating frame of reference is reasonably advocated and fictitious forces such as the centrifugal force, F_c, and the Coriolis force, F_C, have to be taken into account. Since $h \ll R$, the coordinate system used for the derivation of the modified SWE is identical to that used in Section 2.1. In other words, the axial x, tangential θ, and radial r coordinates are mapped (Fig. 2) on the Cartesian plane $(x, \theta, r) \rightarrow (x, y, z)$ as the following

$$x = x, \quad y = R\theta, \quad z = R - r \tag{3}$$

with R the radius of the cylinder. Note that this transformation is only possible when $h \ll R$. The centrifugal acceleration a_c acts purely in the radial direction,

$$a_c = \Omega^2(R - z) \tag{4}$$

with $0 \leqslant z \leqslant h$ and Ω the angular frequency of the mold. Like any other acceleration acting in the radial direction, also the centrifugal acceleration a_c contributes to the hydrostatic pressure p

$$p = a_c \rho (h - z) \tag{5}$$

with h the liquid height, and ρ the liquid density. Then, the gradient of the hydrostatic pressure p can be added to the flux function in (2) as the following:

$$
\begin{aligned}
(hu)_t + \left(hu^2 + \frac{1}{2}\Omega^2 R h^2 - \frac{1}{3}\Omega^2 h^3 \right)_x + (huv)_y &= 0 \\
(hv)_t + (huv)_x + \left(hv^2 + \frac{1}{2}\Omega^2 R h^2 - \frac{1}{3}\Omega^2 h^3 \right)_y &= 0
\end{aligned}
\tag{6}
$$

Note that $h^3 \ll Rh^2$ and therefore, the second term corresponding to the centrifugal acceleration a_c can be neglected. The momentum equations become:

$$
\begin{aligned}
(hu)_t + \left(hu^2 + \frac{1}{2}\Omega^2 R h^2 \right)_x + (huv)_y &= 0 \\
(hv)_t + (huv)_x + \left(hv^2 + \frac{1}{2}\Omega^2 R h^2 \right)_y &= 0
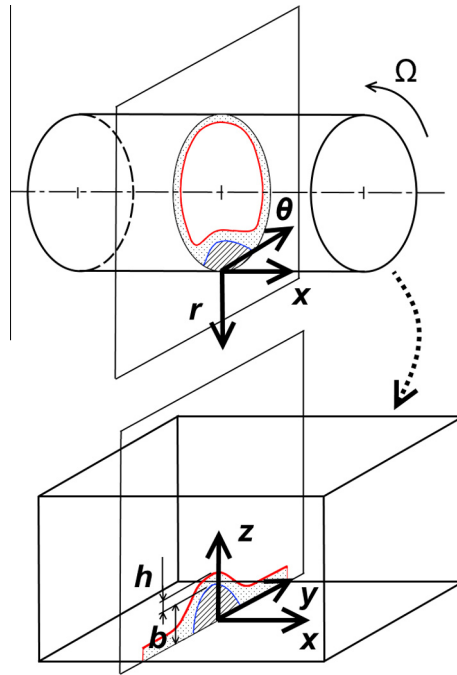\end{aligned}
\tag{7}
$$

Fig. 2. A sketch of the coordinate system transformation.

The centrifugal term $1/2\Omega^2 Rh^2$ in (7) is the analogy to the gravity term $1/2\,gh^2$ in (2). Despite describing the flow in a cylindrical geometry, note that we keep the 2D Cartesian coordinate system for the derivation of the modified SWE, which is justified by having $h \ll R$. To complete the fictitious force terms in (7), the Coriolis force has to be included. Assuming the radial momentum is negligible and the cylinder rotating about its axis, only the radial component of the Coriolis acceleration a_C is nonzero

$$a_C = -2\Omega v \tag{8}$$

In addition, an assumption about the velocity profile in the radial direction is made. On the cylinder wall a no slip boundary condition is considered i.e. $u(0) = 0$ and $v(0) = 0$. On the free surface, a zero stress boundary condition is considered i.e. $\partial u(h)/\partial z = 0$ and $\partial v(h)/\partial z = 0$. Within $0 \leqslant z \leqslant h$, a parabolic velocity profile is constructed with the mass-flow averaged velocity components u and v.

$$u(z) = 3uz(2h - z)/(2h^2) \tag{9}$$

$v(z)$ can be written analogously. Following the steps used for any acceleration acting in the radial direction, the gradient of the corresponding hydrostatic pressure divided by the density ρ, denoted $\boldsymbol{F}_C$, reads

$$\boldsymbol{F}_C = -\frac{5}{2}\Omega h v \begin{bmatrix} h_x \\ h_y \end{bmatrix} - \frac{5}{4}\Omega h^2 \begin{bmatrix} v_x \\ v_y \end{bmatrix} \tag{10}$$

Later, it will be shown in the algorithm part that it is convenient to take a part of the Coriolis force as a flux function and the rest leave as a source term. In addition to the fictitious forces, several more forces have to be included. Starting with the force of gravity, one has to bear in mind the rotating frame of reference used and the rotating vector of the gravitational acceleration $\vec{g}(t)$ consequently.

$$\vec{g}(t) = (0, -g\sin(\Omega t), -g\cos(\Omega t)) \tag{11}$$

with zero axial component and the tangential and the radial component different from zero. Taking the radial component of acceleration first and again calculating the gradient of the corresponding hydrostatic pressure divided by the liquid density, denoted $\boldsymbol{F}_g$, reads

$$\boldsymbol{F}_g = -g\cos(\Omega t)h \begin{bmatrix} h_x \\ h_y \end{bmatrix} \tag{12}$$

After adding the tangential component integrated over the liquid height h

$$\boldsymbol{F}_g = -g\cos(\Omega t)h\begin{bmatrix} h_x \\ h_y \end{bmatrix} - g\sin(\Omega t)\begin{bmatrix} 0 \\ h \end{bmatrix} \tag{13}$$

with t the physical time. Besides, it is no less important to examine various shear stresses that likely appear in the HSC process. In the case of a viscous Newtonian fluid, the bed shear stress is derived from the assumption of a parabolic velocity profile as the following:

$$\boldsymbol{\tau}_b = \boldsymbol{\tau}_\mu = 3\mu/h\begin{bmatrix} u \\ v \end{bmatrix} \tag{14}$$

with μ the dynamic viscosity. If τ_b only includes turbulent and dispersive effects, the bed shear stress takes the form

$$\boldsymbol{\tau}_b = \boldsymbol{\tau}_t = \rho c_f\begin{bmatrix} u|u| \\ v|v| \end{bmatrix} \tag{15}$$

with c_f the friction coefficient. In addition to the bed shear stress τ_b, the liquid can show other types of flow resistance such as a yield stress τ_{yi}. Different types of stresses can be lumped together by a single formula expressing the flow resistance relation. More details about such relations can be found e.g. in [16]. Up to here, the liquid layer was in the contact with the cylindrical wall. However, in the HSC process the solidification takes place from the cylindrical wall and therefore, the underlying topography of the liquid layer varies in time and corresponds to the actual solid height, denoted b. The solid height b naturally affects all the forces resulting from any acceleration acting in the radial direction.

Then, assuming the solid height b greater than zero, the centrifugal force $\boldsymbol{F}_c$ becomes:

$$\boldsymbol{F}_c = -\Omega^2 Rh\begin{bmatrix} h_x \\ h_y \end{bmatrix} - \Omega^2 Rh\begin{bmatrix} b_x \\ b_y \end{bmatrix} \tag{16}$$

Unlike the first term applied inside the flux function (16), the second term with the gradient of the solid height b stays on the right-hand side as a source term. The Coriolis force $\boldsymbol{F}_C$ is altered by the solid height b as the following:

$$\boldsymbol{F}_C = -\frac{5}{2}\Omega h v\begin{bmatrix} h_x \\ h_y \end{bmatrix} - \frac{5}{4}\Omega h^2\begin{bmatrix} v_x \\ v_y \end{bmatrix} - 2\Omega h v\begin{bmatrix} b_x \\ b_y \end{bmatrix} \tag{17}$$

Finally, the gravity force $\boldsymbol{F}_g$ as the last force being affected by the solid height b takes the form

$$\boldsymbol{F}_g = -g\ \cos(\Omega t)h\begin{bmatrix} (h+b)_x \\ (h+b)_y \end{bmatrix} - g\ \sin(\Omega t)\begin{bmatrix} 0 \\ h \end{bmatrix} \tag{18}$$

2.3. Heat advection diffusion equation for modified SWE

The heat advection diffusion equation integrated over the liquid height h has to be solved simultaneously with the modified SWE. For the average temperature T of the liquid layer h the following transport equation holds:

$$hT_t + (huT)_x + (hvT)_y = (h\alpha T_x)_x + (h\alpha T_y)_y + S_T \tag{19}$$

with α the thermal diffusivity and S_T the source term due to solidification and heat transfer to the mold.

2.4. Complete set of equations

The average flow dynamics of the liquid layer inside the horizontally rotating cylinder coupled with the advection diffusion equation for the average temperature of the liquid layer T is mathematically described by the following system of equations:

$$\begin{bmatrix} h \\ hu \\ hv \\ hT \end{bmatrix}_t + \begin{bmatrix} hu \\ hu^2 + \frac{1}{2}\Omega^2 Rh^2 + \frac{5}{4}\Omega vh^2 \\ huv \\ huT \end{bmatrix}_x + \begin{bmatrix} hv \\ huv \\ hv^2 + \frac{1}{2}\Omega^2 Rh^2 + \frac{5}{4}\Omega vh^2 \\ hvT \end{bmatrix}_y = \boldsymbol{S} \tag{20}$$

with $\boldsymbol{S}$ the source terms given by:

$$\boldsymbol{S} = \begin{bmatrix} 0 \\ -\Omega^2 Rhb_x - \frac{5}{4}\Omega h^2 v_x - 2\Omega h v b_x - g\cos(\Omega t)h(h+b)_x - 3\frac{\mu}{\rho}\frac{u}{h} - c_f u|u| - \frac{\tau_{yi}}{\rho} \\ -\Omega^2 Rhb_y - 2\Omega h v b_y - g\cos(\Omega t)h(h+b)_y - g\sin(\Omega t)h - 3\frac{\mu}{\rho}\frac{v}{h} - c_f v|v| - \frac{\tau_{yi}}{\rho} \\ (h\alpha T_x)_x + (h\alpha T_y)_y + S_T \end{bmatrix} \tag{21}$$

2.5. Heat diffusion, solidification, and mold filling

In addition to the average flow dynamics and heat transport of the liquid layer, the heat diffusion inside the cylinder and the continuously solidifying liquid has to be solved with appropriate thermal boundary conditions at the walls and the free surface. Convective and radiative heat losses are taken into account. The solidification of the liquid layer starts exclusively from the inner wall of the cylinder as a moving planar liquid/solid interface. The 3D heat diffusion equation is solved on a finite volume grid in the cylindrical coordinates along with the Stefan condition applied at the liquid/solid interface. The initially empty mold is continuously filled with the hot liquid approximately in the center of the mold. The heat diffusion, the solidification, and the mold filling are out of the scope of this paper and are described in detail in [10].

3. Calculation

3.1. Approximate Riemann solver

The original SWE (1), (2) is a system of strictly hyperbolic non-linear PDEs, whereas (20) is a system of conditionally hyperbolic PDEs due to the presence of the Coriolis term in the flux function. The benefit from applying the Coriolis term in the flux function and not as a source term will be clearly demonstrated later by a 1D numerical test. The homogeneous system of (20) can be symbolically written as

$$\mathbf{Q}_t + \mathbf{A}(\mathbf{Q})_x + \mathbf{B}(\mathbf{Q})_y = \mathbf{0} \tag{22}$$

with $\mathbf{Q}$ the vector of conserved quantities $\mathbf{Q} = [h, \quad hu, \quad hv, \quad hT]^T$ and $\mathbf{A}$ and $\mathbf{B}$ flux functions. The 2D set of Eq. (22) can be broken down to two 1D sets of equations by the dimensional splitting [17].

$$\mathbf{Q}_t + \mathbf{A}(\mathbf{Q})_x = \mathbf{0}$$
$$\mathbf{Q}_t + \mathbf{B}(\mathbf{Q})_y = \mathbf{0} \tag{23}$$

The fluxes $\mathbf{A}(\mathbf{Q})_x$ and $\mathbf{B}(\mathbf{Q})_y$ can be replaced by $\mathbf{A}'(\mathbf{Q})\mathbf{Q}_x$ and $\mathbf{B}'(\mathbf{Q})\mathbf{Q}_y$ respectively with $\mathbf{A}'(\mathbf{Q})$ and $\mathbf{B}'(\mathbf{Q})$ Jacobian matrices. Both Jacobian matrices are diagonalizable with conditionally real eigenvalues $\lambda^{A,B}$ and corresponding eigenvectors.

$$\lambda^A = \left[u - \sqrt{h\left(\Omega^2 R + \tfrac{5}{2}\Omega v\right)}, \quad u + \sqrt{h\left(\Omega^2 R + \tfrac{5}{2}\Omega v\right)}, \quad u, \quad u \right]$$
$$\lambda^B = \left[v + \tfrac{5}{8}\Omega h - \sqrt{h\left(\Omega^2 R + \tfrac{5}{2}\Omega v + \tfrac{25}{64}\Omega^2 h\right)}, \quad v + \tfrac{5}{8}\Omega h + \sqrt{h\left(\Omega^2 R + \tfrac{5}{2}\Omega v + \tfrac{25}{64}\Omega^2 h\right)}, \quad v, \quad v \right] \tag{24}$$

The hyperbolicity of (20) is lost, when any of the eigenvalues (24) is a complex number. From (24), a critical velocity v_c can be calculated

$$v_c = -2/5\Omega R, \tag{25}$$

below which the system of PDEs is no longer hyperbolic. In the HSC process, the order of magnitude of v_c is 10 m/s, which can hardly be reached due to the fact that the liquid rotates nearly at the same speed as the mold. Since the solution procedure is very similar for both, x and y, directions, only the y direction is detailed here. Each eigenvalue corresponds to a finite wave speed at which the information travels through the domain. The first two waves from λ are analogous to nonlinear gravity waves in the original SWE and the last two waves are linearly degenerate. In the tangential (y) direction, the following set of equations is solved

$$\mathbf{Q}_t + \mathbf{B}'(\mathbf{Q})\mathbf{Q}_y = 0 \tag{26}$$

using an approximate Riemann solver. On each face of a 1D grid with a uniform spacing a 1D Riemann problem is solved in order to get the wave strengths $\boldsymbol{\alpha}$ each corresponding to its wave speed λ and eigenvector r. The wave strengths are obtained by solving the system of linear equations

$$\mathbf{r}\boldsymbol{\alpha} = \Delta\mathbf{Q} \tag{27}$$

with $\Delta\mathbf{Q}(= \mathbf{Q}_R - \mathbf{Q}_L)$ the jump in $\mathbf{Q}$ over the cell face and $\mathbf{r}$ being a matrix of column eigenvectors r.

$$\mathbf{r} = \begin{bmatrix} 1 & 1 & 0 & 0 \\ u & u & 1 & 0 \\ \lambda_1 & \lambda_2 & 0 & 0 \\ T & T & 0 & 1 \end{bmatrix} \tag{28}$$

A linearization of $u, \ v, \ T,$ and h is required for both λ and $\mathbf{r}$. A Roe linearization [18] is applied in order to find special averages $\hat{u}, \ \hat{v}, \ \hat{T}$ and $\hat{h}$. The Roe averages of $\hat{u}, \ \hat{T}$ and $\hat{h}$ are identical to those for the original SWE (1), (2), given by:

$$\hat{u} = \frac{\sqrt{h_L}u_L + \sqrt{h_R}u_R}{\sqrt{h_L} + \sqrt{h_R}}, \quad \hat{T} = \frac{\sqrt{h_L}T_L + \sqrt{h_R}T_R}{\sqrt{h_L} + \sqrt{h_R}}, \quad \hat{h} = (h_L + h_R)/2, \tag{29}$$

whereas $\hat{v}$ is modified by adding a correction to the original Roe average.

$$\hat{v} = \frac{\sqrt{h_L}v_L + \sqrt{h_R}v_R}{\sqrt{h_L} + \sqrt{h_R}} + \frac{(v_R - v_L)(\sqrt{h_L}h_R - \sqrt{h_R}h_L)}{2(h_R + h_L)\left(\sqrt{h_R} + \sqrt{h_L}\right)} \tag{30}$$

After using the Roe averages in the matrix of eigenvectors $\mathbf{r}$ (28) the system of linear equations (26) is solved for the wave strengths $\boldsymbol{\alpha}$.

$$\boldsymbol{\alpha} = \left[\frac{\Delta h\lambda_2 - \Delta hv}{\lambda_2 - \lambda_1}, \quad -\frac{\Delta h\lambda_1 - \Delta hv}{\lambda_2 - \lambda_1}, \quad \Delta hu - \hat{u}\Delta h, \quad \Delta hT - \hat{T}\Delta h \right]^T \tag{31}$$

The centrifugal waves are connected by intermediate states h_m and hv_m (Fig. 3) as the following:

$$\begin{aligned}
h_m &= h_L + \alpha_1 \\
h_m &= h_R - \alpha_2 \\
hv_m &= hv_L + \alpha_1\lambda_1 \\
hv_m &= hv_R - \alpha_2\lambda_2
\end{aligned} \tag{32}$$

Approximate Riemann solvers generally do not distinguish between a shock wave and a rarefaction and treat each wave as a shock wave. To treat a subsonic or a supersonic rarefaction as a shock wave usually does not cause any troubles in the solution especially in the case of a narrow rarefaction fan. However, if the rarefaction occurs in the transonic regime, one widely reported problem is the entropy violation resulting in unphysical expansion shocks. In the present paper, the correct solution is restored by applying the Harten–Hyman entropy fix [19].

The source term $\mathbf{S}$ (21) can be applied using several different methods. The fractional-step method [20] is a popular method, in which we alternate between solving a homogeneous conservation law and a simple ODE. This approach is simple to use and implement. However, if the solution is close to a steady state i.e. the gradient of the flux almost balances the source term, which cannot be correctly captured by the fractional-step method. Moreover, the fractional-step method often generates unphysical oscillations in the solution. In the present paper, only the source term S_4 in the heat advection diffusion equation (19) is solved using this method namely the BDF implicit method. The rest of the source term $\mathbf{S}$ (S_1–S_3) is directly included in the Riemann solver as a singular source at each discontinuity without modifying the original solution vector of conserved quantities $\mathbf{Q}$. This approach is said to upwind the source term by means of projecting it onto the matrix of eigenvectors $\mathbf{r}$ and propagating it at the wave speeds λ. As shown in Fig. 3, in the homogeneous case the centrifugal waves are connected by the intermediate states h_m and hv_m, whereas in the nonhomogeneous case with the source terms the intermediate state h_m is split into two intermediate states h_{Lm} and h_{Rm} separated by a stationary jump discontinuity corresponding to
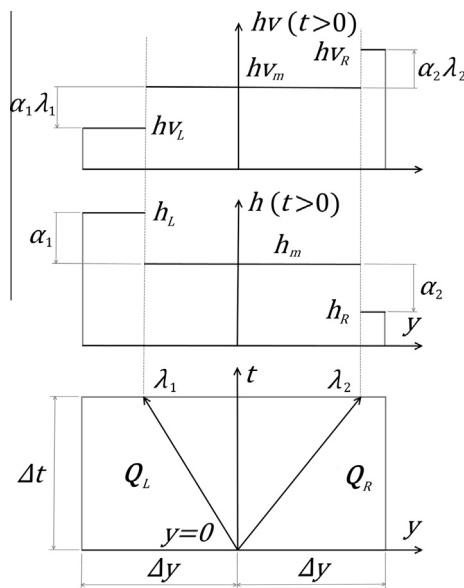

Fig. 3. Solution of the Riemann problem at $y = 0$ without the source term S_3. Discontinuities λ_1 and λ_2 are connected by constant intermediate states h_m and hv_m.

the source term (Fig. 4). The momentum is conserved through the stationary discontinuity meaning that the centrifugal waves λ_1 and λ_2 are still connected by a single intermediate state hv_m (32), however modified by the effect of the source term. In the tangential (y) direction, the following set of nonhomogeneous equations is solved.

$$\mathbf{Q}_t + \mathbf{B}'(\mathbf{Q})\mathbf{Q}_y = [0 \quad 0 \quad S_3 \quad 0]^T \tag{33}$$

The wave speeds λ remain unchanged, while the source strengths $\boldsymbol{\beta}$ are added to the wave strengths $\boldsymbol{\alpha}$

$$\boldsymbol{\beta} = \left[\frac{S_3}{(\lambda_2 - \lambda_1)\lambda_1}, \quad -\frac{S_3}{(\lambda_2 - \lambda_1)\lambda_2}, \quad 0, \quad 0 \right]^T \tag{34}$$

The intermediate states h_{Lm}, h_{Rm}, and hv_m^* become

$$\begin{aligned}
h_{Lm} &= h_L + \alpha_1 + \beta_1 \\
h_{Rm} &= h_R - \alpha_2 - \beta_2 \\
hv_m^* &= hv_L + \alpha_1\lambda_1 + \beta_1\lambda_1 \\
hv_m^* &= hv_R - \alpha_2\lambda_2 - \beta_2\lambda_2
\end{aligned} \tag{35}$$

Even in the less complex case, without the source terms, a Riemann solver linearized using the Roe average can fail completely. It can give a nonphysical solution such as a negative liquid height ($h < 0$) especially when the solution is close to a vacuum state. Using modified wave speeds λ defined according to HLLE solver, which is positively conservative, is a possible remedy. Here, a different approach was however employed in which a minimum liquid height h_{min} was used to identify a threshold for a dry cell. Then, any $h < h_{min}$ and the corresponding velocity v were set to zero when solving the Riemann problem. Note that this procedure is used to determine the solution of the Riemann problem. It does not modify the vector of conserved quantities $\mathbf{Q}$. This approach has been recently advocated e.g. in [21]. When dealing with the source term in (33), the positivity of both, h_{Lm} and h_{Rm}, needs to be checked and an adequate numerical limit has to be applied. In Fig. 5, the limiting strategy is shown for $h_{Lm} < 0$. The source strength β_1 has to be limited as the following

$$\beta_1 = -h_m, \quad \beta_2 = -\beta_1\lambda_1/\lambda_2 \tag{36}$$

Similarly, in case that $h_{Rm} < 0$ the source strength β_2 is modified

$$\beta_2 = h_m, \quad \beta_1 = -\beta_2\lambda_2/\lambda_1 \tag{37}$$

In addition to the numerical limit due to the occurrence of the negative height [22], a physical limit is applied to prevent incorrect evaluation of the friction source term [16] based on the fact that none of the friction terms cannot change the sign of the intermediate state hv_m (32). Therefore, in case that $(hv_m)(hv_m^*) < 0$ the following physical limit has to be applied.

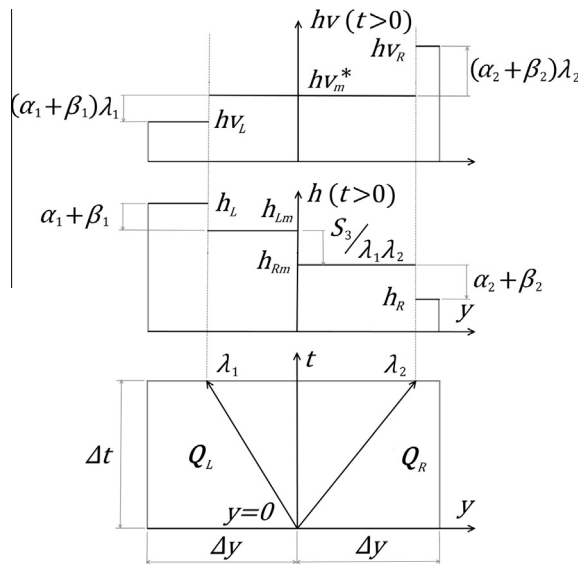$$\beta_1 = -hv_m/\lambda_1, \quad \beta_2 = hv_m/\lambda_2 \tag{38}$$

Fig. 4. Solution of the Riemann problem at $y = 0$ with the source term S_3 as a stationary discontinuity. However, the stationary discontinuity appears only in the liquid height h, separating intermediate states h_{Lm} and h_{Rm}. In the tangential momentum hv still a single intermediate state hv_m^* exists altered by the effect of the source term S_3.
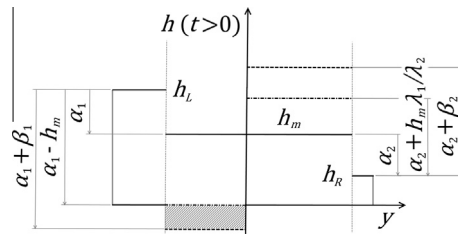
Fig. 5. Negative liquid height h (hatched region) generated by the source strength β_1. A numerical limit $\beta_1 = -h_m$ applied, forcing h_{Lm} to 0.

3.2. Wave-propagation algorithm

After solving the Riemann problem at each face of the cell in the tangential (y) direction, the complete information about the wave speeds λ (24), the matrix of eigenvectors $\boldsymbol{r}$ (28), the wave strengths $\boldsymbol{\alpha}$ (31), and the source strengths $\boldsymbol{\beta}$ (34) is obtained. To update the solution it is straightforward to apply the Godunov's explicit updating formula, which is basically the first order accurate upwind method. To reconstruct the vector of quantities in a cell c_{ij} only waves entering this cell are used to update the solution, whereas waves leaving the cell c_{ij} have no effect. After performing $n + 1$ time steps Δt, the vector of quantities $(\boldsymbol{Q})_{ij}^{n+1}$ reads

$$(\boldsymbol{Q})_{ij}^{n+1} = (\boldsymbol{Q})_{ij}^{n} - \frac{\Delta t}{\Delta y}\left(\boldsymbol{B}^{+}(\Delta \boldsymbol{Q})_{i,j-1/2}^{n} + \boldsymbol{B}^{-}(\Delta \boldsymbol{Q})_{i,j+1/2}^{n}\right) \tag{39}$$

with Δy the grid size in the tangential direction, $\boldsymbol{B}^{+}(\Delta \boldsymbol{Q})_{i,j-1/2}^{n}$ the right going fluctuations, and $\boldsymbol{B}^{-}(\Delta \boldsymbol{Q})_{i,j+1/2}^{n}$ the left going fluctuation corresponding to the waves entering the cell c_{ij} from the left and right respectively, given by the following formulas

$$\begin{aligned}\boldsymbol{B}^{+}(\Delta Q)_{i,j-1/2}^{n} &= \sum_{p:\lambda_p > 0} \lambda_p r_p (\alpha_p + \beta_p) \\ \boldsymbol{B}^{-}(\Delta \boldsymbol{Q})_{i,j+1/2}^{n} &= \sum_{p:\lambda_p < 0} \lambda_p r_p (\alpha_p + \beta_p)\end{aligned} \tag{40}$$

evaluated at the cell faces $f_{i,j-1/2}$ and $f_{i,j+1/2}$ respectively. Although the Godunov's method is non-dispersive and does not produce phase errors in treating the wave speeds, it shows a great deal of a numerical diffusion. In order to avoid the numerical diffusion and dispersion at the same time, so-called high resolution (HR) corrections with flux limiters can be applied, increasing the order of accuracy by assuming a piece-wise linear $\boldsymbol{Q}$ instead of piece-wise constant. On smooth solutions the HR corrections are second order accurate, while at sharp discontinuities, where the flux limiters are applied in order to avoid an overshooting (or dispersion), it is only first order accurate. One of the advantages of this approach is that each wave is upwinded and limited separately which contributes significantly to the overall accuracy of the algorithm. The HR corrections are added to the Godunov's updating formula (39) as the following:

$$(\boldsymbol{Q})_{ij}^{n+1} = (\boldsymbol{Q})_{ij}^{n} - \frac{\Delta t}{\Delta y}\left(\boldsymbol{B}^{+}(\Delta \boldsymbol{Q})_{i,j-\frac{1}{2}}^{n} + \boldsymbol{B}^{-}(\Delta \boldsymbol{Q})_{i,j+\frac{1}{2}}^{n}\right) - \frac{\Delta t}{\Delta y}\left((\boldsymbol{G})_{i,j+1/2}^{n} - (\boldsymbol{G})_{i,j-1/2}^{n}\right) \tag{41}$$

with $\boldsymbol{G}$ the correction term calculated at $f_{i,j-1/2}$ and $f_{i,j+1/2}$ takes the form

$$G = \frac{1}{2}\sum_{p=1}^{4} |\lambda_p|\left(1 - \frac{\Delta t}{\Delta y}|\lambda_p|\right) r_p(\alpha_p + \beta_p)\phi(\theta_p) \tag{42}$$

with $\phi(\theta_p)$ the limiter function located within the TVD region [23]. In the present model, the MC flux limiter was considered [24]. The stability region is controlled by the convective limit CFL (Courant–Friedrichs–Lewy) [25] and the time step Δt is determined as the following:

$$\Delta t = CFL \Delta y / \max|\lambda_p| \tag{43}$$

In case that friction terms (14), (15) are used, $CFL \leqslant 1/2$, else CFL can be increased up to 1.

4. Results and discussion

4.1. Grid size sensitivity study

The grid size sensitivity study was performed on a 1D grid, $2\pi R$ long, with a uniformly spaced grid points (100, 400, or 1000), aligned with the tangential direction i.e. with periodic boundary conditions applied. Eq. (33) was solved without the

heat advection, the Coriolis force, and the source term S except of the term $-\Omega^2 R h b_y$ corresponding to the part of the centrifugal force due to the variable topography b. The chosen initial liquid height h has a parabolic shape given by

$$h(y, t = 0) = \begin{cases} f(y) & \text{if } f(y) \geqslant 0 \\ 0 & \text{otherwise} \end{cases} \tag{44}$$

with $f(y) = 0.1 - 5(y - 1.8)^2$. Also the solid height b has initially a parabolic shape

$$b(y, t = 0) = \begin{cases} g(y) & \text{if } g(y) \geqslant 0 \\ 0 & \text{otherwise} \end{cases} \tag{45}$$

with $g(y) = 0.02 - 1(y - 1.0)^2$.

The initial momentum of the liquid layer is zero ($hv(y, t = 0) = 0$). During $t > 0$, the parabolic liquid column collapses with two shocks propagating to the left and right. The shocks travel through the periodic extremities, pass each other and reflect from the solid obstacle. After 10 s corresponding to multiple reflections of the shocks from the solid obstacle (approximately 20 reflections), the free surface pattern is compared for each grid size. From Fig. 6, it is obvious that after 10 s only a single moving discontinuity remains in the solution. For a larger number of grid points the wave speed error can be neglected.

4.2. Preserving steady state over variable topography

It is well documented that the fractional-step methods for applying source terms can produce inaccurate results especially when the solution is close to a steady state. In the present algorithm, the source terms are however completely embedded inside the approximate Riemann solver and therefore, the well-balancing of the source term S is maintained. A typical test was performed on the lake in rest with a variable topography b. The same equations, the same grid (400 grid points), and initial conditions as in Section 4.1 were used for this test except of the initial distribution of the liquid height, which was given by

$$h(y, t = 0) = 0.4 - b(y, t = 0) \tag{46}$$

In Fig. 7, the y-axis on the left and right shows the total height and velocity, respectively. At $t = 10$ s, the velocity magnitude is everywhere nearly zero, within the round-off error of the algorithm used.

4.3. Stop-and-go mechanism

Although the liquid layer is usually modeled as a Newtonian fluid, a more complicated rheological model might be required when the liquid comprises e.g. a mixture of the liquid metal and free-floating equiaxed crystals. The stop-and-go mechanism is applicable to a non-Newtonian liquid which refuses to flow until a certain level of stress, the yield stress τ_y, is exceeded. Thus by applying a sufficiently large yield stress τ_y in the source term S, the algorithm should be capable of stopping a moving liquid front, all velocities should ultimately decay to zero. The verification of the stop-and-go mechanism was performed on a collapsing parabola given by (44) with $f(y)$ equal to
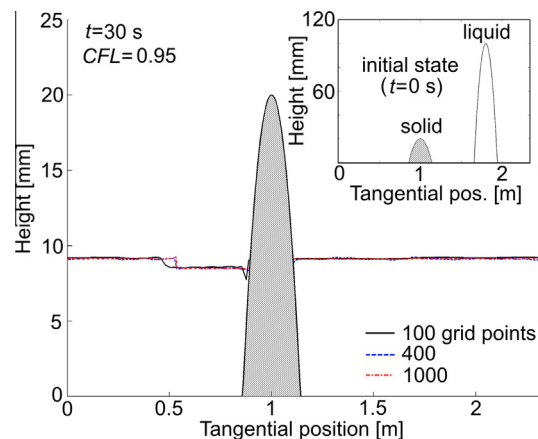
$$f(y) = 0.05 - 5(y - 1.2)^2 \tag{47}$$

Fig. 6. Grid size sensitivity study showing a wave speed error for different number of grid points (100, 400, and 1000 g.p.).
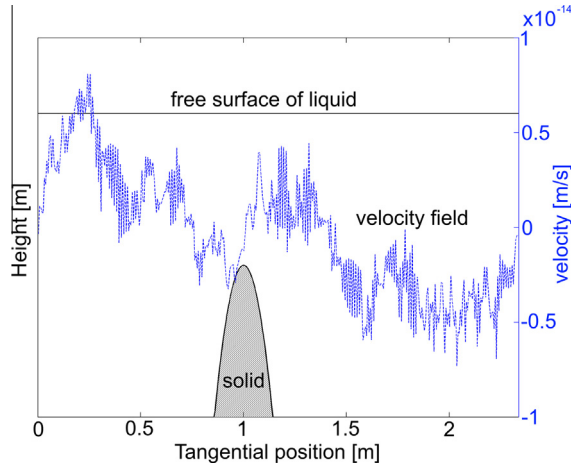
Fig. 7. Preserving steady state over variable topography (a lake in rest). Magnitudes of velocity are nearly zero, within the bounds of the round-off error.

Other parameters and settings were the same as in Section 4.1 except that $b(y, t = 0) = 0$. The yield stress τ_y was defined using the following formula

$$\tau_y = \Omega^2 R \tan(\gamma), \tag{48}$$

meaning that the front of the liquid layer in rest with the density $\rho = 1$ should be inclined by angle γ[rad] at the liquid height $h = 1$. In other words, the liquid does not move and the centrifugal force exactly balances the yield stress ($\rho\Omega^2 Rh\partial h/\partial y = -\tau_y$), which is illustratively shown in Fig. 8.

Here, in the numerical test the angle γ and the density ρ were set to 1° and 6800 kg/m^3 respectively. In Fig. 9, the initial conditions are shown in the upper left corner. In addition, the actual shape of the free surface and the corresponding velocity field is shown at $t = 0.07$ s. Despite a nonzero slope of the free surface in the central part, the liquid already stopped moving there, whereas the fronts still propagate to the left and right. Finally, a steady state is shown at $t = 0.5$ s, at which the centrifugal pressure exactly balances the effect of the yield stress τ_y and therefore the liquid layer shows no movement.

4.4. Coriolis force effect

The Coriolis acceleration a_c has the only nonzero component in the radial direction, pushing the liquid either towards or outwards the cylinder wall depending on whether the liquid velocity v is positive or negative. The best demonstration of the Coriolis effect is again on the collapsing parabola given by (44) with $f(y)$ equal to

$$f(y) = 0.01 - 5(y - 1.2)^2 \tag{49}$$

Other parameters and settings were the same as in Section 4.1 except that $b(y, t = 0) = 0$. In Fig. 10, the dashed lines correspond to the case with the Coriolis force at $t = 0.07$ s. For a better comparison, also the case without the Coriolis force is presented by solid lines. The Coriolis force obviously breaks the symmetry of the collapsing parabola. The liquid naturally propagates faster to the right than to the left.

As shown in Section 2.4, the Coriolis force is put inside the flux function, on the left-hand side of (26), instead of applying it fully as a source term. Both approaches have however their pros and cons. The Coriolis force inside the flux function can turn the eigenvalues from real to complex numbers, meaning that the hyperbolicity can be lost. On the other hand, there is no need for the space integration and any physical or numerical limit, which is generally required when dealing with source
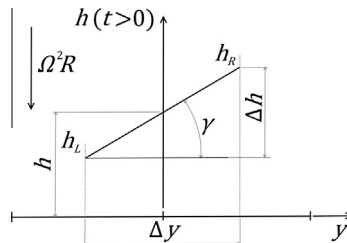

Fig. 8. A schematic of the force balance between the centrifugal force and the yield stress for the liquid height h and the liquid density ρ.
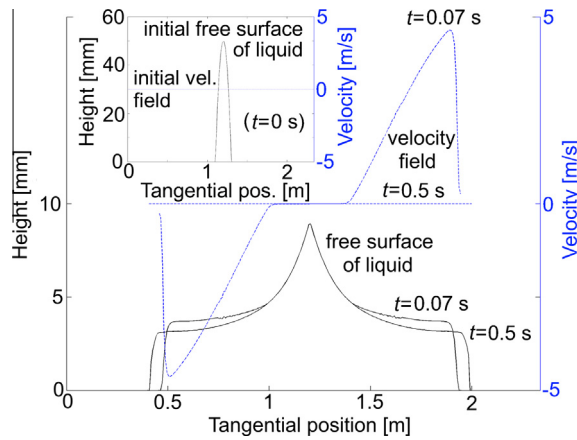
Fig. 9. Initially static liquid parabola collapsing until the balance between the centrifugal pressure and the yield stress τ_y restored.
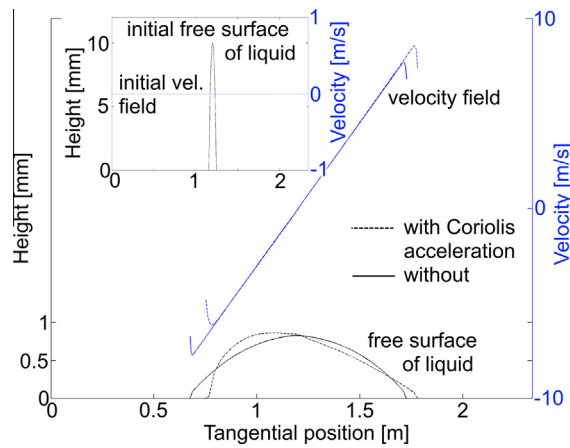

Fig. 10. Effect of the Coriolis force. Dashed and solid lines represent the case with and without the Coriolis force at $t = 0.07$ s.

terms. When treating the Coriolis force as a source term, the hyperbolicity is strictly preserved, however; the integration is not clear because of the appearance of the velocity v in the source term. These two approaches are compared to each other in Figs. 11 and 12. The initial conditions is again a liquid parabola given by (44) with $f(y)$ equal to

$$f(y) = 0.02 - 0.25(y - 1.5)^2 \tag{50}$$

In the early stage ($t = 0.06$ s) of the liquid spreading shown in Fig. 11, both approaches give almost identical results. However, as the time t proceeds, spurious oscillations occur in the case of the Coriolis force applied as a source term and gradually grow in time. Although the spurious oscillations extend over the whole domain, the wave speed error is still negligible. See the comparison in Fig. 12 at $t = 5$ s.

4.5. Heat advection test

The average temperature T of the liquid layer is required for the heat diffusion and solidification model mentioned in Section 2.5. Although hT is a conserved quantity (not T), the algorithm should be also able to recover T without any over/undershooting especially near the dry cells. The heat advection test was performed on the collapsing parabola identical to that used in Section 4.4. The average temperature T of the liquid was set to 100 °C. In order to generalize the numerical test, the parabola was collapsing over a solid hump b given by (45) with $g(y)$ equal to

$$g(y) = 0.005 - 0.25(y - 0.8)^2 \tag{51}$$

In Fig. 13, the liquid is just overtopping the hump b at $t = 0.08$ s and the temperature T is obviously advected correctly, without any over/undershooting.
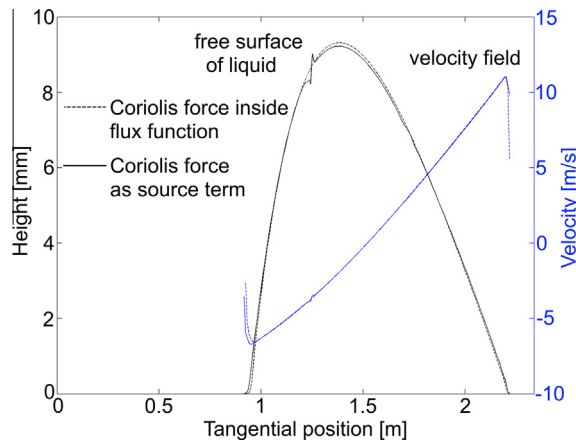
Fig. 11. Coriolis force as a source (the solid line) and as a part of the flux function (the dashed line) at $t = 0.06$ s.
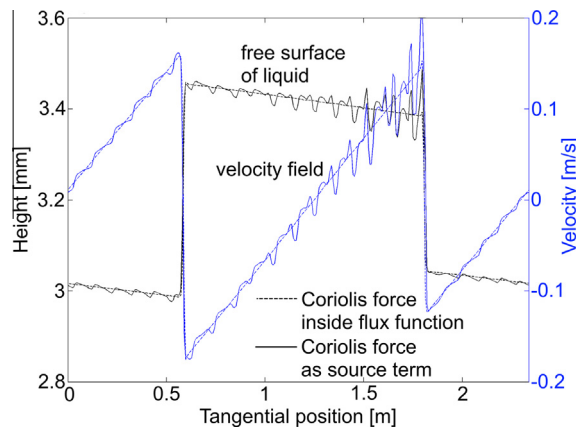

Fig. 12. Coriolis force as a source (the solid line) and as a part of the flux function (the dashed line) at $t = 5$ s.
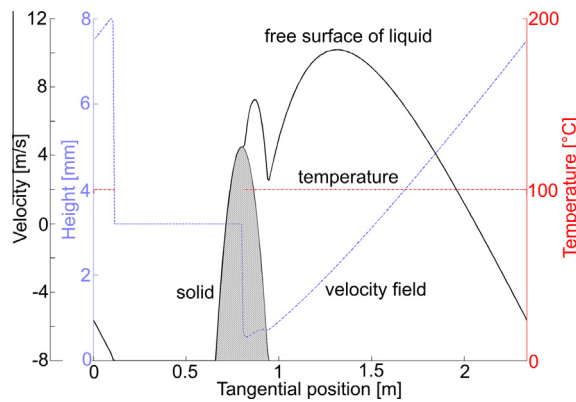

Fig. 13. Heat advection test of a collapsing liquid parabola with the constant temperature of $T = 100\,°C$ at $t = 0.08$ s. The solution is free of under-overshooting in the temperature T, especially near dry cells.

4.6. Full simulation

In addition to the 1D numerical tests discussed in Sections 4.1–4.5, the full set of equations (20) (not only the tangential direction) was solved on a 2D Cartesian grid with the axial and tangential dimension corresponding to the cylinder length L and the cylinder circumference $2\pi R$ respectively. Eq. (20) were simultaneously solved with the heat diffusion and
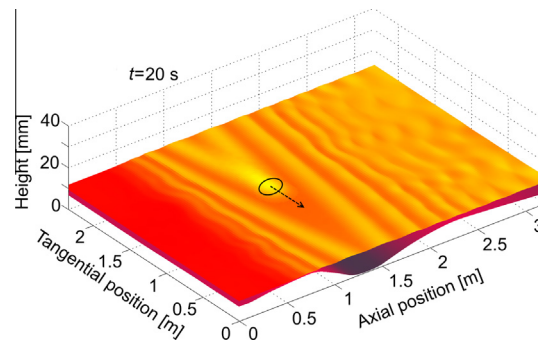
Fig. 14. Contours of the free surface, disturbed by wave patterns, and the liquid/solid interface with the trench formed due to the localized position of the filling jet. At $t = 20$ s, the actual position and the apparent velocity of the filling jet are shown as a solid circle and a dashed arrow.
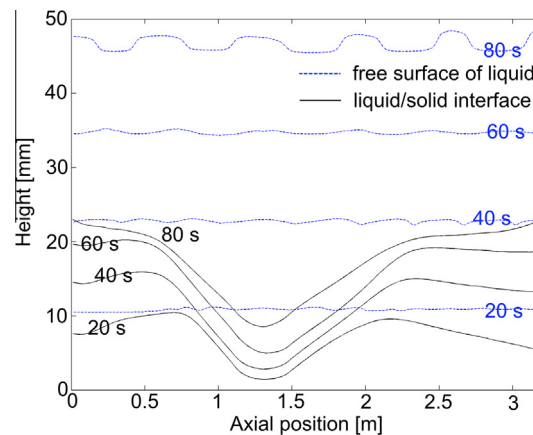
Fig. 15. A time evolution of the free surface (dashed lines) and the liquid/solid interface (solid lines) along the axis of the cylindrical model at the tangential position $y = 1$ m at different times.

solidification model mentioned in Section 2.5. In Fig. 14, the upper and the lower surface represent the actual shape of the free surface of the liquid and the liquid/solid interface respectively at 20 s. Starting with the liquid/solid interface, approximately in the center of the mold (cylinder), exactly bellow the footprint of the filling jet (Fig. 1), the solidification is suppressed due to the newly incoming hot liquid and a trench is formed around the circumference. The actual position of the filling jet is shown as a solid circle with a dashed arrow signifying the apparent velocity of the filling jet. As approaching both extremities of the mold, the solidification rate increases due to the larger distance from the hot filling and increasing radiative heat losses due to the growing view factor between the free surface and the mold opening. The liquid/solid interface continues growing, until the liquid solidifies completely. In the same figure (Fig. 14), the waves are induced by the filling jet and travel mainly in the axial direction, slightly inclined by the effect of the apparently traveling filling jet. The spacing between waves is larger in the vicinity of the filling jet, where the liquid height h is large. On the contrary, the wave spacing is small, when the liquid h is small. The wave spacing is directly linked with the speed of sound, which is proportional to the square root of the liquid height h.

In Fig. 15, the 2D plot shows a time evolution of both, the liquid/solid interface and the free surface, along the axial direction and at the constant tangential position ($y = 1$ m). The liquid/solid interface is not symmetric especially due to the off-centered filling.

5. Conclusions

During the HSC process, a uniform film of liquid layer is formed around a circumference of the cylindrical mold horizontally spinning around its axis of rotation. The liquid layer is not however motionless which is especially caused by the localized filling, the uneven profile of the liquid/solid interface interacting with the gravity force. The liquid flow can be grouped in the category of free surface flows, in which the momentum along the liquid height h is negligible compared to momentum components in other directions, the axial and tangential. Instead of solving a complete set of Navier–Stokes equations, we integrate them over the liquid height h and apply the kinematic boundary condition on the free surface. Only the first order

approximation of the static pressure, the hydrostatic pressure, is considered, leading us to the set of modified shallow water equations (SWE). The modified SWE derived in the present paper include forces such as the centrifugal force, the Coriolis force, the bed shear stress, the yield stress, turbulent and dispersive effects, and variable topography representing the liquid/solid interface. Unlike the original set of SWE, the modified SWE belong to the group of conditionally hyperbolic nonlinear PDEs. In the hyperbolic system shocks and rarefactions propagate at finite wave speeds. In the present paper, an approximate Riemann solver was developed the modified SWE together with the heat advection equation integrated over the liquid height h. To update the solution in time, we adopted explicit updating formulas originally developed by Godunov. The Godunov's method is only first order accurate and due to the piece-wise constant approximation of data the method possesses a significant numerical diffusion. We applied so-called high resolution corrections with flux limiters (MC limiter) so that the order of accuracy was formally increased up to the second order. To update the solution in two space dimensions, we used the simplest Godunov's splitting algorithm to keep the efficiency of the code. In the approximate Riemann solver, the eigenstructure of the SWE was explicitly calculated from the Jacobian matrices linearized with the help of Roe averages. A special correction for the velocity related to the Coriolis force had to be applied in order to fulfill the Roe's linearization. The algorithm was however not depth-positive i.e. negative liquid heights can occur. To prevent negative heights, a minimum liquid height h_{min}, a certain threshold, was defined below which all quantities were set to zero when solving the Riemann problem. All the source terms were included in the Riemann solver as a stationary wave. When a transonic rarefaction was detected, the Harten–Hyman entropy fix was applied in order to prevent expansion shocks. The stability of the explicit algorithm was fully controlled by the convective limit *CFL*. If a rheological model is included, the algorithm is stable for $CFL \leqslant 1/2$. Otherwise, it is possible to use values of *CFL* up to 1.

The capabilities of the algorithm were tested on several 1D simulation. In the grid size sensitivity study (Section 4.1), the wave speed error was qualitatively compared for three different grid sizes, showing only slight differences especially for a larger number of grid points (400 and 1000 g.p.). In Section 4.2, preserving of steady state was verified on the benchmark – the lake in rest with the variable topography b. All velocities were within the round-off error. Note that this is a typical example where the fractional step method for applying a source term would fail. A next 1D numerical test (Section 4.3) was focused on the stop-and-go mechanism applicable when e.g. a yield stress τ_y is considered. An initially patched parabola was collapsing due to the centrifugal force winning over the effect of the yield stress τ_y until a balance between them was restored and a new static shape of the liquid was formed. The main idea of applying any type of friction is a physical limit saying that the friction cannot change the sign of the momentum within each intermediate state (hu_m and hv_m). In Section 4.4, the effect of the Coriolis force was described by means of 1D simulation performed in the tangential direction. Two cases, with and without the Coriolis force, were compared. When only the centrifugal force is applied, the liquid is naturally spreading in a symmetrical manner. Once the Coriolis force comes in the play, the liquid propagates faster when moving in the positive (rotational) direction and vice versa. In addition, a test was performed demonstrating how important is putting the Coriolis force on the left-hand side of the momentum equation and treat it as a part of the flux function. After letting the parabola to collapse, certain waves survive for a very long time because no other force makes them disappear. In the case with the Coriolis as a source term, parasitic oscillations pollute the solution, which does not happen with the Coriolis inside the flux function. The last 1D test (Section 4.5) targeted on testing the performance of the heat advection model fully coupled with the modified SWE, both solved using the Riemann solver. Solving the heat advection equation along with other transport equations (the SWE) using a Riemann solver is only sporadically discussed in the literature. The behavior of the algorithm was checked especially near dry cells, where the over/undershooting in the temperature T would be expected the most. The temperature field was advected correctly, including the region near dry cells. Finally, all the particular properties of the proposed algorithm discussed in Sections 4.1–4.5 were successfully combined in the simulation of the HSC process, a real industrial application (Section 4.6).

Acknowledgments

References

[1] G. Chirita, I. Stefanuscu, J. Barbosa, H. Puga, D. Soares, F.S. Silva, On assessment of processing variables in vertical centrifugal casting technique, Int. J. Cast Met. Res. 22 (2009) 382–389.
[2] C.W. Hirt, B.D. Nichols, Volume of fluid (VOF) method for the dynamics of free boundaries, J. Comput. Phys. 39 (1981) 201–225.
[3] Z. Xu, N. Song, R.V. Tol, Y. Luan, D. Li, Modelling of horizontal centrifugal casting of work roll, Mater. Sci. Eng. 33 (2012) 012030.
[4] E. Kaschnitz, Numerical simulation of centrifugal casting of pipes, Mater. Sci. Eng. 33 (2012) 012031.
[5] K.S. Keerthiprasad, M.S. Murali, P.G. Mukunda, S. Majumdar, Numerical simulation and cold modeling experiments on centrifugal casting, Metall. Mater. Trans. B 42 (2010) 144–155.

[6] L. Drenchev, J. Sobczak, S. Malinoc, W. Sha, Numerical simulation of macrostructure formation in centrifugal casting of particle reinforced metal matrix composites. Part 1: model description, Modell. Simul. Mater. Sci. Eng. 11 (2003) 635–649.

[7] L. Drenchev, J. Sobczak, S. Malinoc, W. Sha, Numerical simulation of macrostructure formation in centrifugal casting of particle reinforced metal matrix composites. Part 2: simulation and practical applications, Modell. Simul. Mater. Sci. Eng. 11 (2003) 651–674.

[8] N. Song, Y. Luan, Y. Bai, Z.A. Xu, X. Kang, D. Li, Numerical simulation of solidification of work roll in centrifugal casting process, J. Mater. Sci. Technol. 28 (2) (2012) 147–154.

[9] A.J.C. Saint-Venant, Théorie du movement non permanent des eaux, avec application aux crues de rivieres et a l'introduction des marrees dans leur lit, C. R. Acad. Sci. Paris 73 (1871) 147–154.

[10] J. Bohacek, A. Kharicha, A. Ludwig, M. Wu, Simulation of horizontal centrifugal casting: mold filling and solidification, ISIJ Int. 54 (2) (2014) 266–274.

[11] D.L. George, Augmented Riemann solvers for the shallow water equations over variable topography with steady states and inundation, J. Comput. Phys. 227 (2008) 3089–3113.

[12] M.-O. Bristeau, B. Coussin, Boundary conditions for the shallow water equations solved by kinetic schemes, Rapport de recherché 4282 (2001) 1–28.

[13] D.L. George, Finite volume methods and adaptive refinement for tsunami propagation and inundation (Ph.D. thesis), submitted at University of Washington, 2006.

[14] E. Audusse, M.-O. Bristeau, B. Perthame, J. Sainte-Marie, A multilayer Saint-Venant system with mass exchanges for shallow water flows. Derivation and numerical validation, ESAIM: Math. Modell. Numer. Anal. 45 (2011) 169–200.

[15] J. Bohacek, A. Kharicha, A. Ludwig, M. Wu, Shallow water model for horizontal centrifugal casting, Mater. Sci. Eng. 33 (2012) 012032 (Int. Conf. MCWSP XIII published in IOP Conf. Series).

[16] J. Murillo, P. Garcia-Navarro, Wave Riemann description of friction terms in unsteady shallows: application to water and mud/debris floods, J. Comput. Phys. 231 (2012) 1963–2001.

[17] R.J. Leveque, Finite Volume Methods for Hyperbolic Systems, Cambridge University Press, New York, 2002 (p. 447).

[18] P.L. Roe, Upwind differencing schemes for hyperbolic conservation laws with source terms, Lect. Notes Math. 1270 (1987) 41–51.

[19] A. Harten, J.M. Hyman, Self-adjusting grid methods for one-dimensional hyperbolic conservation laws, J. Comput. Phys. 50 (1983) 235–269.

[20] R.J. Leveque, Finite Volume Methods for Hyperbolic Systems, Cambridge University Press, New York, 2002 (p. 377).

[21] K. T. Mandli, Finite volume methods for the multilayer shallow water equations with applications to storm surges (Ph.D. thesis) submitted at University of Washington, 2011.

[22] J. Murillo, P. Garcia-Navarro, Weak solutions for partial differential equations with source terms: application to the shallow water equations, J. Comput. Phys. 229 (2010) 4327–4368.

[23] A. Harten, High resolution schemes for hyperbolic schemes for hyperbolic conservation laws, J. Comput. Phys. 49 (1983) 357–393.

[24] B. van Leer, Towards the ultimate conservative difference scheme IV. A new approach to numerical convection, J. Comput. Phys. 23 (1977) 276–299.

[25] R. Courant, E. Isaacson, M. Rees, On the solution of nonlinear hyperbolic differential equations by finite differences, Commun. Pure Appl. Math. 5 (1952) 243–252.